Automotive Innovation (2022) 5:311–323
https://doi.org/10.1007/s42154-022-00187-z

Integrated Path-Following and Fault-Tolerant Control for Four-Wheel Independent-Driving Electric Vehicles

Yuwei Tong[1] · Cong Li[2] · Gang Wang[1] · Hui Jing[1]

Received: 13 November 2021 / Accepted: 4 May 2022 / Published online: 30 June 2022

Abstract
Autonomous vehicles are prone to instability when the motors of the four-wheel independent-driving electric vehicles fail at high driving speed on low-adhesion roads. To improve the vehicle tracking performance in the expected path and ensure vehicle stability when the motor fails, this paper designs an integrated path-following and passive fault-tolerant controller. The path-following controller is designed to improve the vehicle path-following performance based on model predictive control (MPC), while the passive fault-tolerant controller is used to ensure vehicle stability when the motor fails. First, a vehicle dynamic model is established and simplified, and an MPC controller based on a state-space equation is designed. Then, taking the motor fault as a fault factor, a first-order sliding mode fault-tolerant controller is developed. The first-order sliding mode fault-tolerant controller takes the vehicle's yaw rate and sideslip angle into account. Furthermore, to address the chattering problem of the traditional first-order sliding mode fault-tolerant controller, a second-order sliding mode fault-tolerant controller with a disturbance observer is developed. Finally, the developed controller is tested using the Simulink/Carsim platform and applied to a Raspberry Pi 4B for controller hardware-in-the-loop experiment. Simulation and experiment results show the practicability and effectiveness of the proposed integrated control strategy.

Keywords Fault-tolerant control · Model predictive control · Second-order sliding mode control · Path following

Abbreviations

CHIL	Controller hardware-in-the-loop
FTC	Fault-tolerant control
FOSMFTC	First-order sliding mode fault-tolerant controller
FWID-EV	Four-wheel independent-driving electric vehicle
MPC	Model predictive control
MAS	Multi-agent system
NNPID	Neural network proportional–integral–derivative
OPLQR	Optimal preview linear quadratic regulator
SMC	Sliding mode control
SOSMFTC	Second-order sliding mode fault-tolerant controller

Academic Editor: Weichao Zhuang

✉ Hui Jing
jinghui@guet.edu.cn

1 School of Mechanical and Electrical Engineering, Guilin University of Electronic Technology, Guilin, China

2 School of Mechanical Engineering, Guilin University of Aerospace Technology, Guilin, China

1 Introduction

As autonomous driving technology advances, researchers are exploring more flexible and controllable vehicles. The four-wheel independent-driving electric vehicle (FWID-EV) has been studied extensively because of its fast response, high precision, flexibility, energy efficiency, and low emissions [1–3]. The FWID-EV has unique advantages in motor torque control, as it can adapt to different working conditions by directly and accurately controlling the motor output torque, improving the vehicle stability, especially at high speed.

Concurrently, control modes of autonomous vehicles are emerging, among which path-following control is one of the most basic ones considering only traditional working conditions. Zheng et al. [4] proposed a neural network proportional–integral–derivative (NNPID) method, using which the vehicle can follow the desired path with high stability. Hu et al. [5] proposed a robust controller, which considers the uncertainty of parameters and external interference and improves the path-following performance of the automated guided vehicle. A preview model was established in Ref. [6], and an optimal preview linear quadratic regulator (OPLQR) was developed on the basis of the sliding mode control (SMC) strategy. It can realize differential braking by distributing appropriate torque to four wheels during the path-following process. An MPC controller was designed in Ref. [7] to steady the longitudinal velocity and reduce the influence of the longitudinal velocity fluctuation during path following.

Under complex traffic scenarios, it is difficult to maintain vehicle stability with only path-following accuracy being considered, requiring more stability strategies. In Ref. [8], an SMC strategy was developed to ensure vehicle stability by tracking the target yaw rate. According to the path information, the control model predicts the steering angle of the vehicle when it moves laterally to achieve better following performance. A new robust MPC controller was developed in Ref. [9], which can surpass the limitations of the traditional robust MPC in the infinite time domain, thereby improving the path-following accuracy and handling stability of FWID-EV. In Ref. [10], a path re-planning controller and a rear wheel steering stability controller were designed. The zero sideslip angle is considered in the design of the cost function, which improves the trajectory tracking accuracy and maneuverability of the vehicle under some critical working conditions. A multi-agent system (MAS) architecture was developed in Ref. [11], and a Pareto-optimal theory was used to coordinate the direct yaw moment and the front wheel angle output by the controller, through which the vehicle controllability was improved.

A large number of driving motors of electric vehicles suffer from poor working conditions in real-world applications. Motor failure leads to unequal vehicle lateral driving force, resulting in vehicle yaw instability and threatening the safety of the vehicle. Hence, many algorithms have been proposed for fault-tolerant control (FTC) of vehicle drive motor failure. In Ref. [12], a new FTC strategy was designed based on back-stepping control theory, effectively improving the dynamic performance of the motor drive, decreasing torque ripple, and achieving high reliability. A highly reconfigurable architecture was proposed in Ref. [13]. The sliding vector distribution strategy was adopted to ensure the redistribution of torque when the four-wheel motor fails, which enables the tire to work in the linear region. An FTC method based on a cooperative game was designed in Ref. [14]. Four motors were modeled and interacted as four different players to ensure the stability of the FWID-EV when the motor fails. In Ref. [15], for vehicle parameter uncertainties, as well as some disturbances and actuator failure errors, an online update law and feedback law were designed through a triple-step method to improve vehicle stability.

Based on the above research and analysis, an automatic control system can be designed that follows the path, is fault-tolerant, and has strong real-time performance for an unmanned FWID-EV. When the vehicle follows the path, the front wheel angle must be as smooth as possible. More importantly, it must be able to adjust quickly to adapt to changes in trajectory. The MPC control algorithm can realize real-time rolling optimization of control variables and is capable of feedback correction, which can be used to control the vehicle to track the desired path. Moreover, to address vehicle instability due to motor failure and some parameter uncertainties, the SMC algorithm can be considered. The vehicle system is complex and changeable and often includes uncertainty. For example, external disturbances include road and lateral wind disturbances; internal disturbances include constant changes in tire lateral stiffness and other parameters. SMC can handle system disturbances well and has good robustness; therefore, it is often used in vehicle control [16–18]. When the traditional first-order SMC method is used to strengthen the response and anti-jamming capability of the vehicle system, a larger control gain is generally required, which leads to severe chattering, causing harm to the control system. Aiming to resolve the chattering problem caused by the traditional first-order SMC, the second-order SMC method was proposed, which was later proven to be feasible and perform better than the traditional SMC [19–21].

This paper develops an MPC and sliding mode fault-tolerant control integrated controller to solve the problem of vehicle instability when the motor fails. The main contributions of this paper are summarized as follows: (1) In contrast to most studies, which only consider the FTC of electric vehicles or vehicle path-following control, this paper considers both the path-following control and FTC of the vehicle to improve the vehicle stability while presenting effective path-following performance. (2) The second-order sliding mode fault-tolerant controller (SOSMFTC) is designed, and a disturbance observer is used to reduce the fluttering caused by the traditional first-order sliding mode fault-tolerant controller (FOSMFTC), thereby improving the control accuracy.

The remainder of this paper is organized as follows. First, the vehicle planar dynamics model is established in Sect. 2. Then, Sect. 3 describes the design process of the MPC controller and sliding mode FTC controller. A simulation is performed in Simulink/Carsim, and the results are analyzed in Sect. 4. Section 5 reports experimental verification through controller hardware-in-the-loop (CHIL) test. Finally, the conclusions are summarized in Sect. 6.

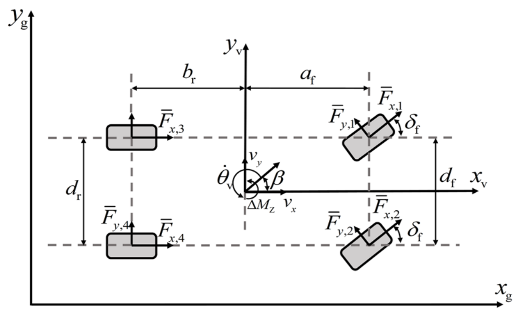

Fig. 1 Vehicle model

2 Description of Vehicle Control Model

2.1 Vehicle Dynamic Model

The vehicle planar dynamic model can accurately reflect vehicle states of lateral, longitudinal, and yaw motion, which makes it indispensable for designing vehicle control algorithms. The force analysis of the vehicle motion state is depicted in Fig. 1, through which the differential equations are determined as follows:

$$m(\dot{v}_x - v_y\dot{\theta}_v) = (\overline{F}_{x,1} + \overline{F}_{x,2})\cos\delta_f - (\overline{F}_{y,1} + \overline{F}_{y,2}) \sin\delta_f + \overline{F}_{x,3} + \overline{F}_{x,4} \tag{1}$$

$$m(\dot{v}_y - v_x\dot{\theta}_v) = (\overline{F}_{y,1} + \overline{F}_{y,2})\cos\delta_f - (\overline{F}_{x,1} + \overline{F}_{x,2}) \sin\delta_f + \overline{F}_{y,3} + \overline{F}_{y,4} \tag{2}$$

$$I_z\ddot{\theta}_v = a_f(\overline{F}_{y,1} + \overline{F}_{y,2})\cos\delta_f + \frac{d_f}{2}(\overline{F}_{y,1} - \overline{F}_{y,2}) \sin\delta_f - b_r(\overline{F}_{y,1} + \overline{F}_{y,2}) + \Delta M_z \tag{3}$$

where ΔM_z can be expressed as

$$\Delta M_z = d_f/2(\overline{F}_{x,1} - \overline{F}_{x,2})\cos\overline{F}_f + a_f(\overline{F}_{x,1} + \overline{F}_{x,2}) \sin\delta_f + d_r/2(\overline{F}_{x,4} - \overline{F}_{x,3}) + \overline{d}(t) \tag{4}$$

where m is the mass of the vehicle; v_x denotes longitudinal speed; v_y denotes lateral speed; $\dot{\theta}_v$ is the actual yaw rate, equal to γ; $\overline{F}_{x,i}$ and $\overline{F}_{y,i}$ are the longitudinal forces and lateral forces of the tire, respectively ($i = 1, 2, 3, 4$, represents the left front wheel, right front wheel, left rear wheel, and right rear wheel, respectively); I_z denotes the rotation inertia of the vehicle; δ_f denotes the front wheel angle of the vehicle; a_f is the distance from the vehicle centroid to the front axles, respectively; d_f and d_r are the track width of the front and rear wheels, respectively; ΔM_z denotes the external yaw moment; $\overline{d}(t)$ denotes the disturbance of vehicle internal uncertainty and external disturbances.

2.2 Vehicle Steady-State Analysis

The γ_d and β_d under steady-state conditions are usually used as expected values to evaluate vehicle stability. Let the actual yaw rate be γ and the actual sideslip angle be β, the vehicle is considered stable when $\gamma \approx \gamma_d$ and $\beta \approx \beta_d$. From Ref. [22], it is known that γ_d and β_d can be described as

$$\gamma_d = \frac{v_x}{(1 + \kappa v_x^2)(a_f + b_r)}\delta_f \tag{5}$$

$$\beta_d = \frac{b_r + m a_f v_x^2}{C_{cr}(1 + \kappa v_x^2)(a_f + b_r)^2}\delta_f \tag{6}$$

where κ is the stability factor; b_r is the distance from the vehicle centroid to the rear axle; C_{cr} denotes the rear tire corning stiffness.

Moreover, since the maximum lateral acceleration $a_{y,\max}$ is limited by the road adhesion coefficient, Eq. (7) must be satisfied [22]:

$$\begin{cases} \left|\hat{\gamma}_{d,\max}\right| \le \dfrac{\mu g}{v_x} \\ \left|\hat{\beta}_{d,\max}\right| \le \mu g\left(\dfrac{b_r}{v_x^2} + \dfrac{m a_f}{C_{cr}(a_f + b_r)}\right) \end{cases} \tag{7}$$

where μ is the road adhesion coefficient.

Thus, the combination of Eq. (6) and Eq. (7) can be rewritten as

$$\gamma_{df} = \min\left\{\left|\gamma_d\right|, \left|\hat{\gamma}_{d,\max}\right|\right\}\mathrm{sgn}(\alpha_f) \tag{8}$$

$$\beta_{df} = \min\left\{\left|\beta_d\right|, \left|\hat{\beta}_{d,\max}\right|\right\}\mathrm{sgn}(\beta_d) \tag{9}$$

3 Controller Design

The controllers in this section include the MPC controller, sliding mode FTC controller, and P controller that produces longitudinal torque through the speed difference to

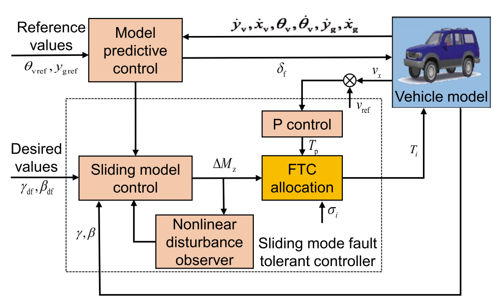

Fig. 2 Framework of the integrated controller

steady the vehicle's longitudinal speed. Here compares the performance of the FOSMFTC and the SOSMFTC when the sliding mode FTC controller is considered. Figure 2 shows the algorithm framework.

3.1 MPC Controller Design

The MPC controller is a path-following controller that enables vehicles to travel along specified paths. The vehicle dynamic model in Sect. 2.1 is simplified based on the assumption of linear tire and wheel deflection at a small angle. The detailed equations are as follows:

$$\begin{cases} m\ddot{y}_v = -m\dot{x}_v\dot{\theta}_v + 2\big[C_{cf}(\delta_f - \dot{y}_v/\dot{x}_v \\ \quad -a_f\dot{\theta}_v/\dot{x}_v) + C_{cr}(b_r\dot{\theta}_v - \dot{y}_v)/\dot{x}_v\big] \\ m\ddot{x}_v = m\dot{y}_v\dot{\theta}_v + 2\big[C_{lf}s_f - C_{cf}(\delta_f - \\ \quad (\dot{y}_v + a_f\dot{\theta}_v)/\dot{x}_v)\alpha_f + C_{lr}s_r\big] \\ I_z\ddot{\theta}_v = 2a_f\big[a_fC_{cf}(\delta_f - \dot{y}_v/\dot{x}_v \\ \quad -a_f\dot{\theta}_v/\dot{x}_v) - b_rC_{cr}(b_r\dot{\theta}_v - \dot{y}_v)/\dot{x}_v\big] \\ \dot{x}_g = \dot{x}_v\cos\theta_v - \dot{y}_v\sin\theta_v \\ \dot{y}_g = \dot{x}_v\sin\theta_v + \dot{y}_v\cos\theta_v \end{cases} \tag{10}$$

where x_v and y_v are the longitudinal and lateral displacement of the vehicle, respectively; C_{cf} and C_{lf} are the front and rear tire longitudinal stiffness, respectively; s_f and s_r are the slip rate of the front and rear wheel; x_g and y_g are the vehicle longitudinal and lateral displacement in the inertial coordinate system, respectively.

Nonlinear control requires complex operation processing, making it hard to guarantee the high stability of the controller. Considering this, Eq. (10) is linearized. First, Eq. (10) is transformed into a state-space form, the state quantity is selected as $\Gamma = [\dot{y}_v\ \dot{x}_v\ \theta_v\ \dot{\theta}_v\ \dot{y}_g\ \dot{x}_g]$, and the front wheel steering $\boldsymbol{\Phi} = \delta_f$ is set as the control input. Next, the nonlinear dynamic equation $\dot{\Gamma}(t) = f(\Gamma(t), \boldsymbol{\Phi}(t))$ is established by Eq. (10). Nonlinear MPC can be designed through nonlinear equations, which could not guarantee high stability. Considering the advantages of linear time-varying MPC, such as simplicity of solutions and low computational costs [23, 24], the first-order Taylor expansion of Eq. (10) is performed at the current working point $(\Gamma(t_0), \Phi(t_0))$, and the linear time-varying equation can be obtained as follows:

$$\dot{\Gamma}(t) = \boldsymbol{R}(t_0)\Gamma(t_0) - \boldsymbol{Z}(t_0)\Phi(t_0) + \boldsymbol{C}(t_0) \tag{11}$$

where $\boldsymbol{R}(t_0) = \begin{bmatrix} \frac{\partial f_{\dot{y}_v}}{\partial \dot{y}_v} & \frac{\partial f_{\dot{y}_v}}{\partial \dot{x}_v} & 0 & \frac{\partial f_{\dot{y}_v}}{\partial \dot{\theta}_v} & 0 & 0 \\ \frac{\partial f_{\dot{x}_v}}{\partial \dot{y}_v} & \frac{\partial f_{\dot{x}_v}}{\partial \dot{x}_v} & 0 & \frac{\partial f_{\dot{x}_v}}{\partial \dot{\theta}_v} & 0 & 0 \\ 0 & 0 & 0 & 1 & 0 & 0 \\ \frac{\partial f_{\dot{\theta}_v}}{\partial \dot{y}_v} & \frac{\partial f_{\dot{\theta}_v}}{\partial \dot{x}_v} & 0 & \frac{\partial f_{\dot{\theta}_v}}{\partial \dot{\theta}_v} & 0 & 0 \\ \cos\theta_v & \sin\theta_v & \frac{\partial f_{\dot{x}_g}}{\partial \theta_v} & 0 & 0 & 0 \\ -\sin\theta_v & \cos\theta_v & \frac{\partial f_{\dot{y}_g}}{\partial \theta_v} & 0 & 0 & 0 \end{bmatrix}$,

$\boldsymbol{Z}(t_0) = \left[\frac{2C_{cf}}{m}, \frac{-2C_{cf}}{m}\left(2\alpha_f - \frac{\dot{y}_v + a_f\dot{\theta}}{\dot{x}_v}\right), 0, \frac{2a_fC_{cf}}{I_z}, 0, 0\right]$,

$\boldsymbol{C}(t_0) = \Gamma(t_0) - \boldsymbol{R}(t_0)(\Gamma) - \boldsymbol{Z}(t_0)\Phi(t_0)$.

In order to solve Eq. (11) iteratively, it is discretized using the forward Euler method. Then, the following equation can be derived:

$$\begin{cases} \Gamma_{k+1,t} = \boldsymbol{R}_{k,t}\Gamma_{k,t} + \boldsymbol{Z}_{k,t}\boldsymbol{\Phi}_{k,t} + d_{k,t} \\ \boldsymbol{Y}_{k,t} = \boldsymbol{Q}_{k,t}\Gamma_{k,t} + \boldsymbol{N}_{k,t}\boldsymbol{\Phi}_{k,t} + e_{k,t} \end{cases} \tag{12}$$

where $\boldsymbol{R}_{k,t} = \boldsymbol{I} + T\boldsymbol{R}(t_0)$ and $\boldsymbol{Z}_{k,t} = T\boldsymbol{Z}(t_0)$ ($\boldsymbol{I}$ represents a unit matrix and T represents the sampling step).

In order to effectively constrain the increment of the control system, Eq. (12) is converted into an increment type:

$$\begin{cases} \hat{\Gamma}_{k+1,t} = \hat{\boldsymbol{R}}_{k,t}\hat{\Gamma}_{k,t} + \hat{\boldsymbol{Z}}_{k,t}\Delta\boldsymbol{\Phi}_{k,t} + \hat{\boldsymbol{C}}_{k,t} \\ \boldsymbol{Y}_{k,t} = \hat{\boldsymbol{Q}}_{k,t}\hat{\Gamma}_{k,t} + \hat{\boldsymbol{N}}_{k,t}\Delta\boldsymbol{\Phi}_{k,t} + \boldsymbol{E}_{k,t} \end{cases} \tag{13}$$

where $\hat{\Gamma}_{k+1,t} = \begin{bmatrix} \Gamma_{k,t} \\ \boldsymbol{\Phi}_{k-1,t} \end{bmatrix}$, $\hat{\boldsymbol{R}}_{k,t} = \begin{bmatrix} \boldsymbol{R}_{k,t} & \boldsymbol{Z}_{k,t} \\ \boldsymbol{0}_{m\times n} & \boldsymbol{I}_m \end{bmatrix}$, $\hat{\boldsymbol{Z}}_{k,t} = \begin{bmatrix} \boldsymbol{Z}_{k,t} \\ \boldsymbol{I}_m \end{bmatrix}$, $\hat{\boldsymbol{N}}_{k,t} = \boldsymbol{N}_{k,t}$, $\hat{\boldsymbol{C}}_{k,t} = \begin{bmatrix} \boldsymbol{C}_{k,t} \\ \boldsymbol{0}_m \end{bmatrix}$, $\Delta\boldsymbol{\Phi}_{k,t} = \boldsymbol{\Phi}_{k,t} - \boldsymbol{\Phi}_{k-1,t}$, $\hat{\boldsymbol{Q}}_{k,t} = [\,\boldsymbol{Q}_{k,t}\ \boldsymbol{N}_{k,t}\,]$ (where $\boldsymbol{I}_m$ denotes a matrix with m rows of 1, $\boldsymbol{0}_m$ denotes a matrix with m columns of 0, and $\boldsymbol{0}_{m\times n}$ denotes a matrix with m rows and n columns of 0).

There are two important measurement parameters when the vehicle follows the path: the heading angle and the lateral displacement. In addition, considering that control variables and control increments should be optimal, a cost function can be designed as follows:

$$\begin{aligned} J_{\min}&\left(\hat{\Gamma}(t), \boldsymbol{\Phi}(t-1), \Delta\Xi(t), \omega\right) \\ &= \sum_{i=1}^{Np}\left\|\boldsymbol{Y}(t+i|t) - \boldsymbol{Y}_{ref}(t+i|t)\right\|_{Q_1}^2 \\ &+ \sum_{i=0}^{Nc-1}\|\Delta\boldsymbol{\Phi}(t+i|t)\|_{R_1}^2 \\ &+ \sum_{i=0}^{Nc-1}\|\boldsymbol{\Phi}(t+i|t)\|_S^2 + \rho\omega^2 \end{aligned} \tag{14}$$

where $\Delta\Xi(t) = [\Delta\varpi(t), \cdots, \Delta\varpi(t+N_c-1)]$, $\boldsymbol{Y}_{ref} = [\theta_{vref}, y_{gref}]$, ω is the relaxation factor, and $\varepsilon \geq 0$; N_p represents the prediction step length; N_c represents the control step length; and $\boldsymbol{Q}_1$, $\boldsymbol{R}_1$, $\boldsymbol{S}$, ρ represent the weight factors of the tracking error, control increment, control amount, and relaxation factor, respectively.

The physical meaning of Eq. (27) is explained below. The first item is used to ensure accurate tracking of the lateral displacement and heading angle in vehicle path following. The second item is used to produce an optimal front wheel angle increment to prevent severe shaking. The third item is used to generate a better front wheel angle. The last item is used to prevent the calculation from being unsolvable by adjusting the relaxation factor.

Combining Eq. (14) and the constraint conditions, the optimization problem of this dynamic model predictive controller can be described as follows:

$$\min_{\Delta\boldsymbol{\Phi}(t),\varepsilon} \boldsymbol{J}_{\min}(\hat{\Gamma}(t), \boldsymbol{\Phi}(t-1), \Delta\Xi(t), \omega)$$
$$s.t \begin{cases} \hat{\Gamma}_{k+1,t} = \hat{\boldsymbol{R}}_{k,t}\hat{\Gamma}_{k,t} + \hat{\boldsymbol{Z}}_{k,t}\Delta\boldsymbol{\Phi}_{k,t} + \hat{\boldsymbol{C}}_{k,t}, k = t, \cdots, t+N_p-1 \\ \boldsymbol{Y}_{k,t} = \hat{\boldsymbol{Q}}_{k,t}\hat{\Gamma}_{k,t} + \hat{\boldsymbol{N}}_{k,t}\Delta\boldsymbol{\Phi}_{k,t} + \boldsymbol{E}_{k,t}, k = t, \cdots, t+N_p-1 \\ \boldsymbol{\Phi}_{k,t} = \boldsymbol{\Phi}_{k-1,t} + \Delta\boldsymbol{\Phi}_{k,t}, k = t, \cdots, t+N_c-1 \\ \Delta\boldsymbol{\Phi}_{k,t} = 0, k = t+N_c, \cdots, t+N_p \\ \boldsymbol{\Phi}_{\min} \le \boldsymbol{\Phi}_{k,t} \le \boldsymbol{\Phi}_{\max}, k = t+N_c, \cdots, t+N_p \\ \Delta\boldsymbol{\Phi}_{\min} \le \Delta\boldsymbol{\Phi}_{k,t} \le \Delta\boldsymbol{\Phi}_{\max}, k = t, \cdots, t+N_c-1 \\ \omega \ge 0 \end{cases} \tag{15}$$

Equation (15) can be converted into a standard quadratic programming form and solved in MATLAB.

3.2 Sliding Mode FTC Controller Design

An intelligent electric vehicle, when running on a wet road at a high speed, can easily sideslip if the motor fails. In this section, a sliding mode FTC controller is designed to improve the stability of the vehicle. The structure of the sliding mode FTC controller is as follows. The P controller produces longitudinal torque through the speed difference to maintain the vehicle's longitudinal speed. The SMC layer produces additional yaw moment to improve vehicle stability. The FTC allocation layer appropriately distributes the longitudinal torque and additional yaw torque and outputs the torque to the four motors of the vehicle.

(1) Design of P controller. The longitudinal controller of the system is presented as follows:

$$T_p = (v_{ref} - v_x) \cdot K_p \tag{16}$$

where T_p is the torque produced by the P controller, v_{ref} is the reference value of the speed, and K_p is gain constant.

(2) Design of FOSMFTC. Considering that the control goal is to ensure that the actual values of the yaw rate and the sideslip angle are close to their ideal values, the sliding surface is designed as follows:

$$s = \gamma - \gamma_{df} + k(\beta - \beta_{df}) \tag{17}$$

where k is a positive weight factor, which denotes the influence of the sideslip angle deviation in Eq. (17).

From the derivation of Eq. (17), the following can be obtained:

$$\dot{s} = \dot{\gamma} - \dot{\gamma}_{df} + k(\dot{\beta} - \dot{\beta}_{df}) \tag{18}$$

Combining Eq. (18) with Eq. (3), the following is obtained:

$$\dot{s} = \frac{1}{I_z}\Big[a_f(\overline{F}_{y,1} + \overline{F}_{y,2})\cos\delta_f + \frac{d_f}{2}(\overline{F}_{y,1} - \overline{F}_{y,2}) \sin\delta_f - b_r(\overline{F}_{y,3} + \overline{F}_{y,4}) + \Delta M_Z + W_1(t)\Big] \tag{19}$$

where $W_1(t) = I_z[k(\dot{\beta} - \dot{\beta}_{df}) - \dot{\gamma}_{df}]$. $\dot{\beta}_{df}$ and $\dot{\gamma}_{df}$ are bound, and there exists a constant $\overline{W}_1$ satisfying $|W_1(t)| \le \overline{W}_1$.

Based on Eq. (19), the direct yaw moment can be presented as

$$\Delta M_Z = -\varepsilon_1 \cdot \mathrm{sign}(s) - k_1 s - a_f(\overline{F}_{y,1} + \overline{F}_{y,2})\cos\delta_f + b_r(\overline{F}_{y,3} + \overline{F}_{y,4}) - d_f(\overline{F}_{y,1} - \overline{F}_{y,2})\sin\delta_f \big/ 2 \tag{20}$$

where $\varepsilon_1 > \overline{W}_1$, $k_1 > 0$.

Theorem 1 *Suppose that Eq. (20) is satisfied, the sliding variable s will converge to* 0 *in finite time.*

Proof Substituting Eq. (20) into Eq. (19) yields

$$\dot{s} = \frac{-\varepsilon_1 \cdot \mathrm{sign}(s) - k_1 s + W_1(t)}{I_z} \tag{21}$$

The Lyapunov function $V_1(s) = s^2/2$ is defined; taking its derivative and substituting Eq. (21) into it yields

$$\begin{aligned} \dot{V}_1 &= s\dot{s} \\ &= \frac{-\varepsilon_1 \cdot \mathrm{sign}(s) \cdot s - k_1 s^2 + W_1(t)s}{I_z} \\ &\le \frac{-\varepsilon_1|s| - k_1 s^2 + |W_1(t)||s|}{I_z} \\ &\le \frac{-(\varepsilon_1 - \overline{W}_1)}{I_z}|s| \end{aligned} \tag{22}$$

$\varepsilon_1 > \overline{W}_1$ and $V(s) \le s^2/2$, $|s| \ge \sqrt{2}V_1^{\frac{1}{2}}$ and $\dot{V}_1 \le -(\varepsilon_1 - \overline{W})\sqrt{2}V_1^{\frac{1}{2}} \big/ I_z$. The system, therefore, satisfies the finite-time Lyapunov stability theory [25], the sliding variable s will converge to 0 in finite time, and the convergence time T_c satisfies $T_c \le \sqrt{2} I_z V_1^{\frac{1}{2}}(0) \Big/ (\overline{W} - \varepsilon_1)$.

To ensure that the additional yaw moment can be reasonably distributed, the FTC allocation layer is designed. The ratio of the force currently experienced by the tire to the maximum torque it can provide is usually used to describe the tire utilization rate [26], which can be described by the following equation:

$$\lambda_i = \frac{\sqrt{\overline{F}_{x,i}^2 + \overline{F}_{y,i}^2}}{\mu_i \overline{F}_{z,i}} \tag{23}$$

where λ_i represents the tire utilization rate, and the value range is [0,1].

Expected longitudinal torque and additional yaw moment are controlled:

$$\boldsymbol{v} = (T_p, \Delta M_Z)^T \tag{24}$$

The torque of the four wheels allocated by the FTC allocation is used as the control input, which must satisfy

$$\boldsymbol{v} = \boldsymbol{B}\boldsymbol{\Phi}_1 \tag{25}$$

where $\boldsymbol{\Phi}_1 = (T_1, T_2, T_3, T_4)^T$, $\boldsymbol{B} = \begin{pmatrix} \sigma_1, & \sigma_2, & \sigma_3, & \sigma_4 \\ -\frac{d_f \sigma_1}{2R}, & -\frac{d_f \sigma_2}{2R}, & -\frac{d_r \sigma_3}{2R}, & -\frac{d_r \sigma_4}{2R} \end{pmatrix}$, σ_i is the motor fault factor, and the value range is [0,1].

The minimum objective function is established based on the sum of the squares of the four-tire utilization rates. Considering that the tire lateral force $\overline{F}_{y,i}$ is uncontrollable, the lateral force is omitted. The optimization objective function $\boldsymbol{J}_1$ is expressed by the following formula:

$$\boldsymbol{J}_1 = \sum \left(\frac{\sigma_i T_i}{\mu_i \overline{F}_{z,i} R} \right)^2 \tag{26}$$

where μ_i represents the tire-road adhesion coefficient, which is considered to be equivalent to μ; $\overline{F}_{z,i}$ is the vertical load of the tire.

Equation (25) needs to satisfy Eq. (24) and physical constraints, so the optimization problem is written as

$$\begin{aligned} &\min \boldsymbol{J}_1 = \boldsymbol{\Phi}_1^T \boldsymbol{H} \boldsymbol{\Phi}_1 + (\boldsymbol{v} - \boldsymbol{B}\boldsymbol{\Phi}_1)^T \boldsymbol{W} (\boldsymbol{v} - \boldsymbol{B}\boldsymbol{\Phi}_1) \\ &s.t \quad \boldsymbol{\Phi}_{1\min} \le \boldsymbol{\Phi}_1 \le \boldsymbol{\Phi}_{1\max} \end{aligned} \tag{27}$$

where $\boldsymbol{W} = diag(W_{Texp}, W_{\Delta M})$, $\boldsymbol{H} = diag(\sigma_1^2 \Big/ (\mu \overline{F}_{x,1} R), \sigma_2^2 \Big/ (\mu \overline{F}_{x,2} R), \sigma_3^2 \Big/ (\mu \overline{F}_{x,3} R), \sigma_4^2 \Big/ (\mu \overline{F}_{x,4} R))$.

The physical meaning of Eq. (27) is explained below. The first formula is used to ensure the optimal total output torque. The second formula is used to adjust $W_{\Delta M}$ to improve the vehicle stability and adjust W_{Texp} to steady the longitudinal speed.

(3) Design of SOSMFTC with a disturbance observer: In this design, the design of the FTC allocation layer is kept unchanged, but the sliding mode control layer is changed.

Equation (19) can be rewritten as follows:

$$\dot{s} = a_1 + b_1 u_1 \tag{28}$$

where $u_1 = \Delta M_z$ is the control variable, $b_1 = 1 \big/ I_z$, and a_1 is expressed as follows:

$$\begin{aligned} a_1 = \frac{1}{I_z} \Big[& a_f(\dot{\overline{F}}_{y,1} + \dot{\overline{F}}_{y,2}) \cos\delta_f - a_f(\overline{F}_{y,1} + \overline{F}_{y,2}) \sin\delta_f \dot{\delta}_f \\ & + d_f(\dot{\overline{F}}_{y,1} - \dot{\overline{F}}_{y,2}) \sin\delta_f \Big/ 2 + d_f(\overline{F}_{y,1} - \overline{F}_{y,2}) \\ & \cos\delta_f \dot{\delta}_f \big/ 2 - b_r(\dot{\overline{F}}_{y,3} + \dot{\overline{F}}_{y,4}) + \dot{W}_1(t) \Big] \end{aligned} \tag{29}$$

where a_1 is at least locally bounded. Therefore, there exists a positive real number $\overline{a}_1$ satisfying $|a_1| \le \overline{a}_1$.

Then, u_1 can be defined as follows:

$$u_1 = \left[-\beta_1 |s|^{1/2} \mathrm{sign}(s) - \beta_2 \int_0^t \mathrm{sign}(s) \mathrm{d}t \right] \Bigg/ b_1 \tag{30}$$

where $\beta_2' > \beta_1'^3 + \overline{a}_1^2 \cdot (4\beta_1' - 8) \Big/ [\beta_1' \cdot (4\beta_1' - 8)]$, $\beta_1' > 2$.

Let $\beta_2' = \beta_2 / b_1$, $\beta_1' = \beta_1' / b_1$.

Theorem 2 *Supposing that Eq. (30) is satisfied, the sliding variable s will converge to* 0 *in finite time*.

Proof Combining Eq. (28) and Eq. (30), the following formulas can be obtained:

$$\begin{cases} \dot{s} = -\beta_1' |s|^{1/2} \mathrm{sign}(s) + \omega_1 \\ \dot{\omega}_1 = -\beta_2' \mathrm{sign}(s) + \dot{a}_1 \end{cases} \tag{31}$$

The positive definite matrix $\boldsymbol{Z}$ is defined as

$$\boldsymbol{Z} = \frac{1}{2} \begin{bmatrix} 4\beta_2' + \beta_1'^2 & -\beta_1' \\ -\beta_1' & 2 \end{bmatrix} \tag{32}$$

The quadratic Lyapunov function is selected as

$$V_2(s, \omega_1) = \boldsymbol{\zeta}^T \boldsymbol{Z} \boldsymbol{\zeta} \tag{33}$$

where $\boldsymbol{\zeta}^T = [\ |s|^{1/2} \mathrm{sign}(s) \ \ \omega_1 \ ]$.

Taking the derivative of $\boldsymbol{\zeta}$ yields

$$\dot{\boldsymbol{\zeta}} = \frac{1}{|s|^{1/2}} (\boldsymbol{A}_1 \boldsymbol{\zeta} + \boldsymbol{B}_1 \tilde{\dot{a}}_1) \tag{34}$$

The derivative of Eq. (33) can be written as

$$
\begin{aligned}
\dot{V}_2(s,\omega_1) &= 2\dot{\zeta}^{\mathrm{T}}\boldsymbol{Z}\zeta \\
&= \frac{1}{|s|^{1/2}}(2\zeta^{\mathrm{T}}\boldsymbol{A}_1^{\mathrm{T}} + 2\tilde{a}_1\boldsymbol{B}_1^{\mathrm{T}})\boldsymbol{Z}\zeta \\
&\le \frac{1}{|s|^{1/2}}(2\zeta^{\mathrm{T}}\boldsymbol{A}_1^{\mathrm{T}}\boldsymbol{Z}\zeta + 2\tilde{a}_1\boldsymbol{B}_1^{\mathrm{T}}\boldsymbol{Z}\zeta \\
&\quad + \overline{a}_1^2|s| - \tilde{a}_1^2) \\
&= \frac{1}{|s|^{1/2}}(2\zeta^{\mathrm{T}}\boldsymbol{A}_1^{\mathrm{T}}\boldsymbol{Z}\zeta + 2\tilde{a}_1\boldsymbol{B}_1^{\mathrm{T}}\boldsymbol{Z}\zeta \\
&\quad + \overline{a}_1^2\zeta^{\mathrm{T}}\boldsymbol{C}_1^{\mathrm{T}}\boldsymbol{C}_1\zeta + \zeta^{\mathrm{T}}\boldsymbol{Z}\boldsymbol{B}_1\boldsymbol{B}_1^{\mathrm{T}}\boldsymbol{Z}\zeta) \\
&\le \frac{1}{|s|^{1/2}}(\zeta^{\mathrm{T}}\boldsymbol{A}_1^{\mathrm{T}}\boldsymbol{Z}\zeta + \zeta^{\mathrm{T}}\mathbf{Z}\mathbf{A}_1\zeta + \\
&\quad \overline{a}_1^2\zeta^{\mathrm{T}}\boldsymbol{C}_1^{\mathrm{T}}\boldsymbol{C}_1\zeta + \zeta^{\mathrm{T}}\mathrm{Z}\mathrm{B}_1\boldsymbol{B}_1^{\mathrm{T}}\boldsymbol{Z}\zeta) \\
&= \frac{1}{|s|^{1/2}}\zeta^{\mathrm{T}}(\boldsymbol{A}_1^{\mathrm{T}}\boldsymbol{Z} + \mathrm{Z}\boldsymbol{A}_1 + \overline{a}_1^2\boldsymbol{C}_1^{\mathrm{T}}\boldsymbol{C}_1 \\
&\quad + \mathbf{Z}\mathbf{B}_1\boldsymbol{B}_1^{\mathrm{T}}\boldsymbol{Z})\zeta
\end{aligned}
\tag{35}
$$

where $\boldsymbol{A}_1 = \begin{bmatrix} -\frac{1}{2}\beta_1' & \frac{1}{2} \\ -\beta_1' & 0 \end{bmatrix}$, $\boldsymbol{B}_1 = \begin{bmatrix} 0 & 1 \end{bmatrix}^{\mathrm{T}}$, $\boldsymbol{C}_1 = \begin{bmatrix} 1 & 0 \end{bmatrix}$, and $\tilde{a}_1 = |s|^{1/2}\dot{a}_1$.

Let $\boldsymbol{Q}_2 = -(\boldsymbol{A}_1^{\mathrm{T}}\mathbf{Z} + \mathbf{Z}\boldsymbol{A}_1 + \overline{a}_1^2\boldsymbol{C}_1^{\mathrm{T}}\boldsymbol{C}_1 + \mathbf{Z}\boldsymbol{B}_1\boldsymbol{B}_1^{\mathrm{T}}\mathbf{Z})$, then

$$
\dot{V}_2(s,\omega_1) \le -\frac{1}{|s|^{1/2}}\zeta^{\mathrm{T}}\boldsymbol{Q}_2\zeta \tag{36}
$$

where $\boldsymbol{Q}_2 = \begin{bmatrix} \beta_1'\beta_2' + \frac{\beta_1'^3}{2} - \overline{a}_1^2 - \frac{\beta_1'^2}{4} & \frac{\beta_1'}{2} - \frac{\beta_1'^2}{2} \\ \frac{\beta_1'}{2} - \frac{\beta_1'^2}{2} & \frac{\beta_1'}{2} - 1 \end{bmatrix}$.

By the properties of the Schur complement [27], $\boldsymbol{Q}_2$ is a positive definite matrix when $\beta_1' > 2$, $\beta_2' > \beta_1'^3 + \overline{a}_1^2 \cdot (4\beta_1' - 8) \big/ [\beta_1' \cdot (4\beta_1' - 8)]$, and $\beta_1' > 2$, then $\dot{V}_2(s,\omega_1) < 0$.

According to Lemma 2 in Ref. [28], the sliding variable s will converge to 0 in finite time and the convergence time T_{c}' satisfies $T_{\mathrm{c}}' \le \frac{2\sqrt{\beta_{1\max}'(\mathbf{Z})}}{\beta_{1\min}'(\mathbf{Q}_2)}V_2^{\frac{1}{2}}(s(0),\omega_1(0))$.

Let $s = y_1$ and $\dot{s} = y_2$, then Eq. (28) can be derived as

$$
\begin{cases} \dot{y}_1 = y_2 \\ \dot{y}_2 = \dot{a}_1 + b_1\dot{u}_1 \end{cases} \tag{37}
$$

Let $\mathbf{y} = [y_1, y_2]^{\mathrm{T}}$, then Eq. (37) can be rewritten as

$$
\dot{\boldsymbol{y}} = f(\boldsymbol{y}) + \boldsymbol{g}_1\dot{u}_1 + \boldsymbol{g}_2\dot{a}_1 \tag{38}
$$

where $\boldsymbol{g}_1 = [0, b_1]^{\mathrm{T}}$, $\boldsymbol{g}_2 = [0,1]^{\mathrm{T}}$, $f(\boldsymbol{y}) = [y_2, 0]^{\mathrm{T}}$.

The disturbance observer can be designed by Ref. [29] as follows:

$$
\begin{cases} \dot{p} = -\boldsymbol{K}\boldsymbol{g}_2 p - \boldsymbol{K}[\boldsymbol{g}_2\boldsymbol{K}\boldsymbol{y} + f(\boldsymbol{y}) + \boldsymbol{g}_1\dot{u}_1] \\ \dot{\hat{a}}_1 = p + varvecKy \end{cases} \tag{39}
$$

where $\hat{a}_1$ is the estimate of a_1, $\boldsymbol{K} = [k_1, k_2]$.

The external yaw moment ΔM_Z can be derived as

$$
\Delta M_Z = \left[-\beta_1|s|^{1}/2\mathrm{sign}(s) - \beta_2\int_0^t(\mathrm{sign}(s))\mathrm{d}t - \hat{a}_1 \right] \Big/ b_1 \tag{40}
$$

4 Simulation and Analysis

To analyze the performance of controllers, three simulations are performed in Simulink/Carsim. The vehicle parameters are listed in Table. 1.

A standard double-lane change test on slippery pavement (where μ=0.3) is designed in Carsim, where the initial longitudinal velocity v_x of the vehicle is set to 72 km/h. When analyzing simulation results, M_1 represents the left front wheel motor, M_2 is the right front wheel motor, M_3 represents the left rear wheel motor, and M_4 is the right rear wheel motor. The design concepts of these three simulations are described as follows:

(1) ***Case 1:*** The results of the first simulation are compared with other simulation data, showing the control performance of the MPC-FOSMFTC and the MPC-SOSMFTC. The four motors of the vehicle are always normal (where σ_1=1, σ_2=1, σ_3=1 and σ_4=1).
(2) ***Case 2:*** The second simulation exhibits the robustness of the MPC-SOSMFTC in the case of a partial failure of the motor on the opposite side of the vehicle. At 3 s, M_2 and M_3 of the vehicle partially failed (where $\sigma_1 = 1$, $\sigma_2 = 0.5$, $\sigma_3 = 0.3$, and $\sigma_4 = 1$).
(3) ***Case 3:*** The third simulation validates the robustness of the MPC-SOSMFTC in the case of partial faults of the motor on the same side of the vehicle. At 5 s, M_1

Table 1 Vehicle parameters

Parameter	Value
m/kg	1704.7
a_{f}/m	1.035
b_{r}/m	1.655
d_{f}/m	1.565
d_{r}/ m	1.565
C_{cf}/(N·rad^{-1})	−93,642
C_{cr}/(N·rad^{-1})	−73,392
R/ m	0.32
I_z/ (kg·m^2)	3408.1

and M_3 of the vehicle partially failed (where $\sigma_1 = 0.6$, $\sigma_2 = 1$, $\sigma_3 = 0.3$, and $\sigma_4 = 1$).

First, the most intuitive control parameters are analyzed: vehicle trajectory $x_g y_g$, β, and γ. In Fig. 3, the vehicle paths under different cases are plotted. When only the MPC controller is used, the vehicle cannot track the expected path at around 134 m. This is because the MPC algorithm is unable to find a feasible solution owing to the severe sideslip of the vehicle. However, the vehicle trajectory under the MPC-FOSMFTC and the proposed MPC-SOSMFTC can achieve path following. For vehicle trajectory in ***case 1***, the maximum error of the proposed MPC-SOSMFTC is approximately 0.27 m, and that of the MPC-FOSMFTC is approximately 0.66 m. Compared with the latter, the former is reduced by 59%. For the proposed MPC-SOSMFTC, the maximum error of ***case 2*** is approximately 0.37 m, and that of ***case 3*** is approximately 0.53 m. It is worth noting that the results in ***case 2*** and ***case 3*** perform slightly worse than the MPC-SOSMFTC control results in ***case 1***. This is because when the vehicle motor fails, the control performance of the controller will be slightly decreased; however, as the error in these results is negligible, high vehicle stability can still be achieved. Furthermore, MPC-SOSMFTC in ***case 3*** and ***case 2*** demonstrates better control performance than MPC-FOSMFTC in ***case 1***.

In Fig. 4(a), the comparison curves of β are plotted. The comparison curves of γ are plotted in Fig. 4(b). There is instability when only the MPC controller is used, as shown in Fig. 4(a) and (b). β and γ suddenly increase at a certain time, far beyond the stable range. However, β and γ are kept within a stable range under FOSMFTC and SOSMFTC. After calculation and analysis, some detailed data can be obtained. In ***case 1***, comparing the results of SOSMFTC and FOSMFTC, the maximum value of β is reduced by approximately 17.1%. For the SOSMFTC, compared with the FOSMFTC results in ***case 1***, the maximum value in ***case 2*** is reduced by approximately 13.5% and that in ***case 3*** is reduced by approximately 11.2%. In ***case 1***, comparing the results of SOSMFTC and FOSMFTC, the maximum value of γ is reduced by approximately 39.8%. For the SOSMFTC,

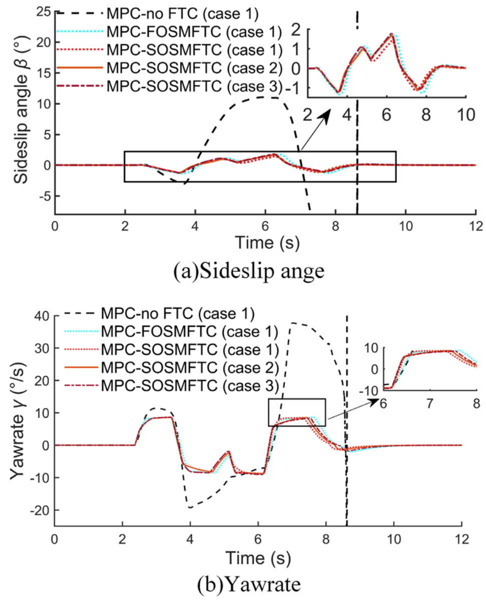

Fig. 4 Sideslip angle and yaw rate

compared with the FOSMFTC results in ***case 1***, the result in ***case 2*** is reduced by about 28.6% and ***case 3*** is reduced by approximately 14.6%. From the above analysis, it can be concluded that the proposed MPC-SOSMFTC presents better control performance than MPC-FOSMFTC. In addition, it should be noted that when the vehicle motor fails, the control accuracy of the proposed MPC-SOSMFTC has only a small error, which is within a reasonable range. Therefore, the above analysis shows that the proposed MPC-SOSMFTC shows better robustness during motor failure.

Next, the control output direct yaw moment ΔM_Z, torque and vehicle speed v_x are analyzed. In ***case 1***, the additional yaw moment ΔM_Z obtained is recorded; as illustrated in Fig. 5, the FOSMFTC has a severe chattering problem, while the proposed controller can solve this problem. According to the calculation, the chattering value is reduced by approximately 94.6%. The torque under FOSMFTC and SOSMFTC is also recorded, as shown in Fig. 6(a) and (b), respectively. As illustrated in the figures,

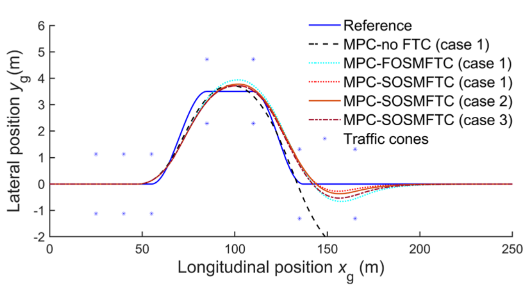

Fig. 3 Trajectory of the vehicle

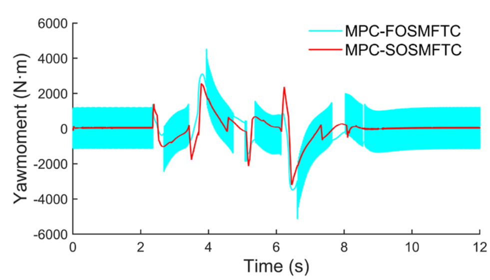

Fig. 5 Direct yaw moment ΔM_Z of ***case 1***

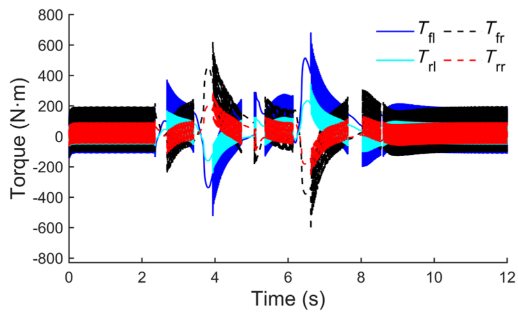

(a)Torque under FOSMFTC

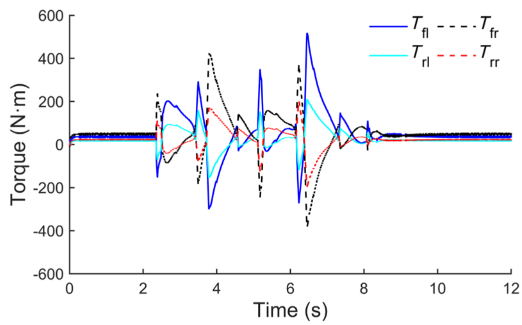

(b)Torque under SOSMFTC

Fig. 6 Torque under FOSMFTC and torque under SOSMFTC (***case 1***)

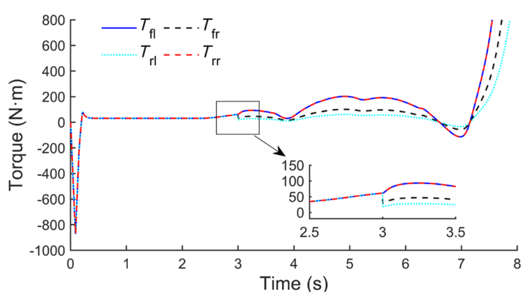

Fig. 7 Longitudinal torque in ***case 2***

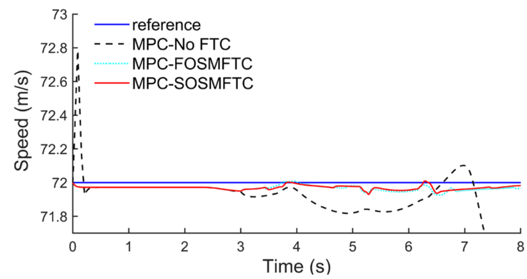

Fig. 8 Speed v_x of the vehicle in ***case 2***

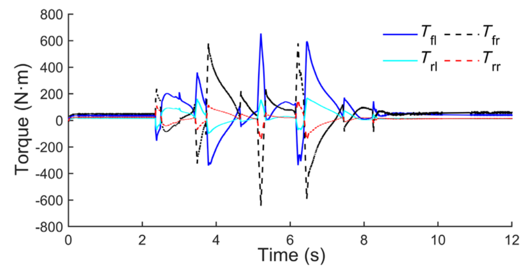

(a)Torque under SOSMFTC

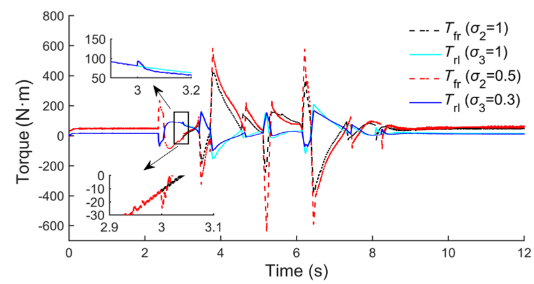

(b)Torque comparison

Fig. 9 Torque under SOSMFTC and torque comparison between motor failure and non-failure (***case 2***)

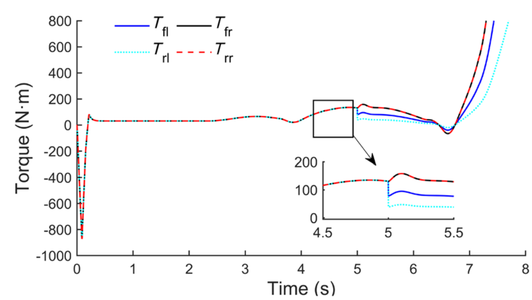

Fig. 10 Longitudinal torque in ***case 3***

the torque under FOSMFTC also has a severe chattering problem, while the proposed controller effectively reduces the chattering of torque.

The longitudinal torque under the P controller in ***case 2*** is recorded; as shown in Fig. 7, the output torque of M_2 and M_3 of the vehicle decreases at 3 s, because of insufficient power invoked by the partial failure of the vehicle motor without FTC. The vehicle speed v_x in ***case 2*** is plotted in Fig. 8. When FTC does not work, v_x cannot be maintained at 3 s, showing a downward trend. However, the proposed controller can still ensure a stable vehicle speed. The torque of the motor under the proposed controller in ***case 2*** is shown in Fig. 9(a), and a torque comparison between motor failure and non-failure cases is plotted in Fig. 9(b). In Fig. 9(a), when the motor fails, the torques of the four motors increase to achieve high vehicle stability. According to Fig. 9(b), M_2 and M_3 fail at 3 s, and the output torque increases significantly.

The longitudinal torque under the P controller in ***case 3*** is plotted in Fig. 10. At 5 s, the longitudinal torque decreases owing to the motor failure. The vehicle speed in ***case 3*** is plotted in Fig. 11. The speed begins to decrease when the vehicle has no FTC, while the proposed controller can maintain a stable speed. The torque of the motor under the proposed controller in ***case 3*** is shown in Fig. 12(a). The torque in motor failure and non-failure cases is compared, as illustrated in Fig. 12(b). Owing to the failure of M_2 and M_3, the calculated output torque increases at 5 s. From the above analysis, it is concluded that when the motor fails, the proposed control algorithm can reasonably adjust the size of the torque to maintain high vehicle stability.

5 Test Validation

5.1 Test Platform Design

To apply the algorithm in the real-world vehicle, a CHIL system is established. The CHIL test scheme is provided in Fig. 13(a) and the CHIL physical diagram in Fig. 13(b). As Fig. 13(b) shows, the main devices include mobile power, a laptop, a display, and a Raspberry Pi 4B as the core hardware. The main steps of the CHIL test are as follows. First, the control algorithm model is built in Simulink. Then, the algorithm model is converted into C code, which is compiled and run on the Raspberry Pi 4B. Finally, the ROS communication module is built in Simulink/Carsim, which is responsible for receiving the torque and angle information delivered by the Raspberry Pi 4B and sending vehicle status information to the Raspberry Pi 4B. As illustrated in Fig. 13(a), the Raspberry Pi 4B and MATLAB are in the same local network. Finally, the calculation results from the Raspberry Pi 4B are transmitted to Simulink through ROS communication.

5.2 CHIL Test Results

The standard double-lane change condition on slippery pavement (where μ=0.3) is designed. In Carsim, the speed of

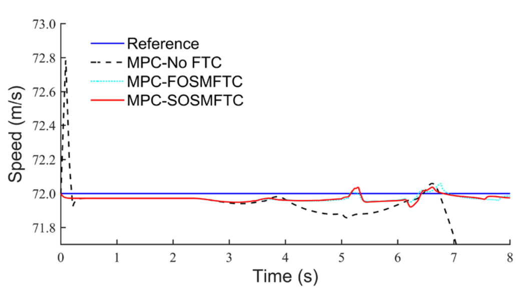

Fig. 11 Vehicle speed v_x in ***case 3***

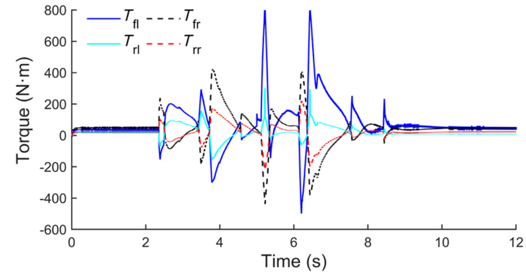

(a)Torque under SOSMFTC

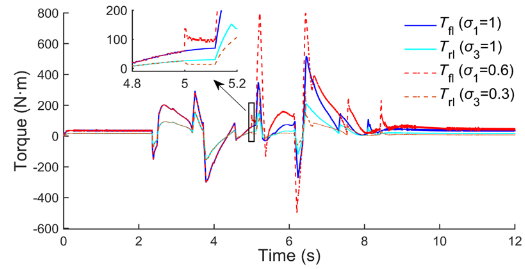

(b)Torque comparison

Fig. 12 Torque under SOSMFTC and torque comparison between motor failure and non-failure (***case 3***)

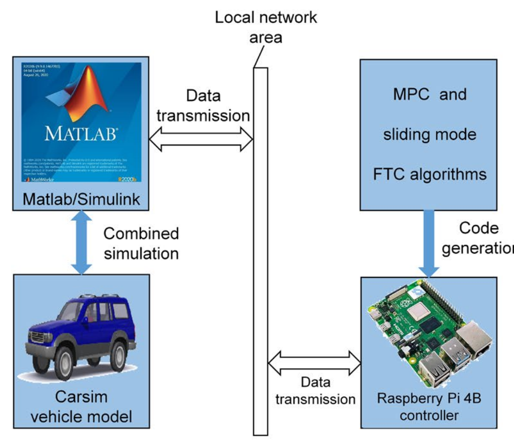

(a)CHIL test scheme

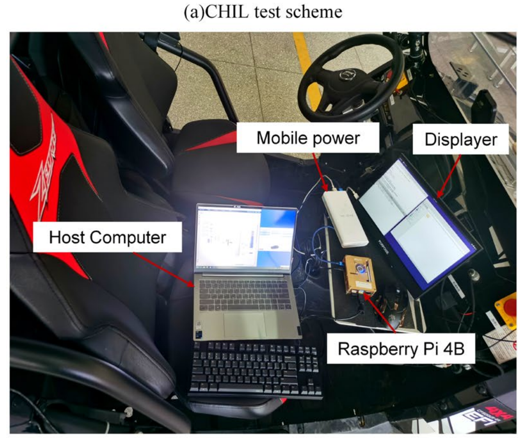

(b)CHIL physical diagram

Fig. 13 CHIL test scheme and CHIL physical diagram the vehicle at the initial position is set to 72 km/h. At 4 s, M_4 fails completely (where $\sigma_1 = 1$, $\sigma_2 = 1$, $\sigma_3 = 1$, and $\sigma_4 = 0$).

The trajectory of the vehicle under different controllers is plotted in Fig. 14. As illustrated in Fig. 14, when the MPC controller is used, the vehicle cannot track the expected path at approximately 134 m. The vehicle can eventually follow the required trajectory under the action of the MPC-FOSMFTC and the proposed MPC-SOSMFTC. When there is no motor failure, the maximum error of MPC is approximately 0.28 m. When the motor fails, the maximum error of the proposed MPC-SOSMFTC is approximately 0.36 m, and that of MPC-FOSMFTC is approximately 0.53 m. The conclusions obtained from the above data are essentially in agreement with that from the simulation results in Sect. 4. The proposed MPC-SOSMFTC can ensure the vehicle stability as much as possible while ensuring that the vehicle follows the path, and the control effect is better than that of MPC-FOSMFTC. The values of β are shown in Fig. 15(a), and those of γ are shown in Fig. 15(b). As demonstrated in the figures, when M_4 fails completely, the proposed MPC-SOSMFTC can still ensure that β and γ are within a steady area. Compared with FOSMFTC, SOSMFTC reduces the error of β by approximately 17.6% under normal vehicle motor conditions. When the motor fails, the comparison error is reduced by 11.8%. For γ, SOSMFTC and FOSMFTC reduce the maximum error by approximately 19.0% and 8.7%, respectively.

The torque of the motor under SOSMFTC is depicted in Fig. 16(a). The torque between motor failure and non-failure is compared in Fig. 16(b). According to Fig. 16(b), M_4 fails completely at approximately 4.1 s because of network delay, but this does not significantly alter the effect of the proposed controller. At 6.5 s, the torque allocated by M_2 increases to maintain vehicle stability. The experimental data indicate that the proposed MPC-SOSMFTC has high real-time capability and robustness.

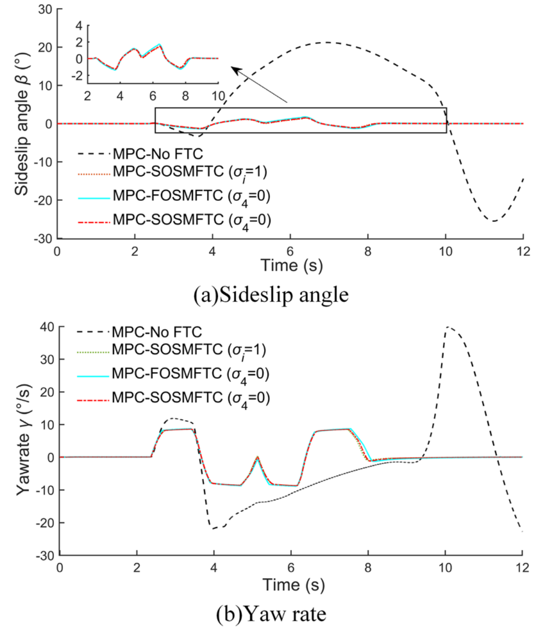

Fig. 15 Sideslip angle and yaw rate

6 Conclusions

This paper develops an integrated controller of path-following control and FTC to improve the path-following performance and stability of the FWID-EV with failed motor. The main results include the following. First, an MPC controller is developed to achieve the accurate vehicle

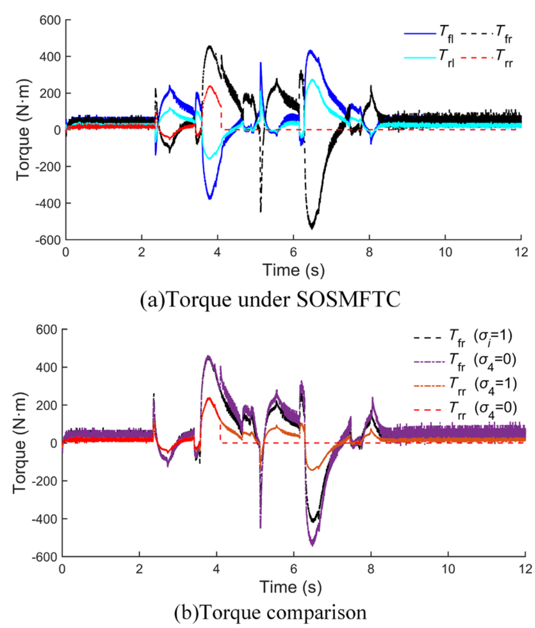

Fig. 16 Torque under SOSMFTC and torque comparison between motor failure and non-failure

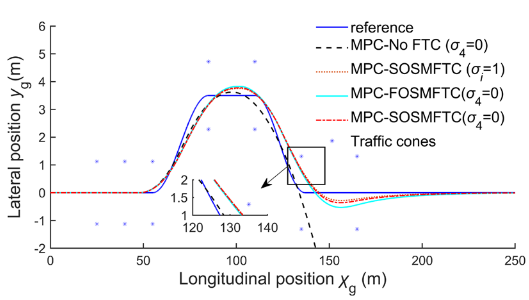

Fig. 14 Trajectory of the vehicle

path following. Second, a SOSMFTC with a disturbance observer is designed, which can effectively reduce the severe chattering of the control quantity caused by the traditional FOSMFTC and enhance the stability of the faulted vehicle. Third, the optimal control allocation method can appropriately allocate the motor torque when the motor fails. Finally, the simulation and CHIL test results show that the proposed integrated controller has better robustness compared to MPC-FOSMFTC. The proposed integrated controller can track the expected path and improve stability when the motor fails, thus improving vehicle path-following performance and stability.

Although the proposed algorithm has been verified by the CHIL test, more conditions should be considered and tested using real vehicles. Future research will focus on how to introduce more hardware devices such as motors and steering wheels, and how to combine them with controllers to perform comprehensive hardware-in-the-loop experiments.

Acknowledgements This work was partly supported by Natural Science Foundation of Guangxi Province, (2020GXNSFAA297031, 2021AA04006), National Natural Science Foundation of China (51605108), and Innovation Project of Guilin University of Electronic Technology (2021YCXS007).

Declarations

Conflict of interest On behalf of all the authors, the corresponding author states that there is no conflict of interest.

References

1. Lv, C., Liu, Y., Hu, X., Guo, H., Cao, D., Wang, F.: Simultaneous observation of hybrid states for cyber-physical systems: a case study of electric vehicle powertrain. IEEE Trans. Cybern. **48**, 2357–2367 (2018)
2. Xing, Y., Lv, C.: Dynamic state estimation for the advanced brake system of electric vehicles by using deep recurrent neural networks. IEEE Trans. Ind. Electron. **67**, 9536–9547 (2020)
3. Huang, Y., Ding, H., Zhang, Y., Wang, H., Cao, D., Xu, N., Hu, C.: A motion planning and tracking framework for autonomous vehicles based on artificial potential field elaborated resistance network approach. IEEE Trans. Ind. Electron. **67**, 1376–1386 (2020)
4. Zheng, H., Yang, S.: A Trajectory tracking control strategy of 4WIS/4WID electric vehicle with adaptation of driving conditions. Appl. Sci. **9**(1), 168 (2019)
5. Hu, C., Jing, H., Wang, R., Yan, F., Chadli, M.: Robust H-infinity output-feedback control for path following of autonomous ground vehicles. Mech. Syst. Signal Process. **70**(71), 414–427 (2016)
6. Zhang, X., Zhu, X.: Autonomous path tracking control of intelligent electric vehicles based on lane detection and optimal preview method. Expert Syst. Appl. **121**, 38–48 (2018)
7. Yao, Q., Tian, Y.: A model predictive controller with longitudinal speed compensation for autonomous vehicle path tracking. Appl. Sci. **9**(22), 4739 (2019)
8. Shen, W., Pan, Z., Li, M., Peng, H.: A lateral control method for wheel-footed robot based on sliding mode control and steering prediction. IEEE Access **6**, 58086–58095 (2018)
9. Peng, H., Wang, W., An, Q., Xiang, C., Li, L.: Path tracking and direct yaw moment coordinated control based on robust MPC with the finite time horizon for autonomous independent-drive vehicles. IEEE Trans. Veh. Technol. **69**(6), 6053–6066 (2020)
10. Chen, Y., Chen, S., Ren, H., Gao, Z., Liu, Z.: Path tracking and handling stability control strategy with collision avoidance for the autonomous vehicle under extreme conditions. IEEE Trans. Veh. Technol. **69**(12), 1–1 (2020)
11. Liang, J., Lu, Y., Yin, G., Fang, Z., Zhuang, W., Ren, Y., Xu, L., Li, Y.: A distributed integrated control architecture of AFS and DYC based on MAS for distributed drive electric vehicles. IEEE Trans. Veh. Technol. **70**(6), 1–1 (2021)
12. Mossa, M., Echeikh, H.: A novel fault tolerant control approach based on backstepping controller for a five phase induction motor drive: experimental investigation. ISA Trans. **112**, 373–385 (2020)
13. Amato, G., Marino, R.: Reconfigurable slip vectoring control in four in-wheel drive electric vehicles. Actuators **10**(7), 157 (2021)
14. Zhang, B., Lu, S.: Fault-tolerant control for four-wheel independent actuated electric vehicle using feedback linearization and cooperative game theory. Eng. Pract. **101**, 104510 (2020)
15. Yang, C., Shi, Y., Li, L., Wang, X.: Efficient mode transition control for parallel hybrid electric vehicle with adaptive dual-loop control framework. IEEE Trans. Veh. Technol. **69**, 1519–1532 (2020)
16. Dai, Y., Ni, S., Xu, D., Zhang, L., Yan, X.: Disturbance-observer based prescribed-performance fuzzy sliding mode control for PMSM in electric vehicles. Eng. Appl. Artif. Intell. **104**, 104361 (2021)
17. Ni, J., Hu, J., Xiang, C.: Envelope Control for four-wheel independently actuated autonomous ground vehicle through AFS/DYC integrated control. IEEE Trans. Veh. Technol. **66**(11), 9712–9726 (2017)
18. Kommuri, S.K., Defoort, M., Karimi, H.R., Veluvolu, K.C.: A robust observer-based sensor fault-tolerant control for PMSM in electric vehicles. IEEE Trans. Ind. Electron. **63**(12), 7671–7681 (2016)
19. Matraji, I., Al-Durra, A., Haryono, A., Al-Wahedi, K., Abou-Khousa, M.: Trajectory tracking control of skid-steered mobile robot based on adaptive second order sliding mode control. Control Eng. Pract. **72**, 167–176 (2018)
20. Tuan, L.A., Joo, Y.H., Tien, L.Q., Duong, P.X.: Adaptive neural network second-order sliding mode control of dual arm robots. Int. J. Control Autom. Syst. **15**, 2883–2891 (2017)
21. Benedikt, A., Elias, H., Ferdinand, S.: Second order sliding modes control for rope winch based automotive driver robot. Int. J. Vehicle Design. **62**(2), 147 (2013)
22. Rajamani, R.: Vehicle Dynamics and Control. Springer, New York (2006)
23. Harati, E.: Toolbox for Nonlinear Model Predictive Controllers. Chalmers University of Technology, Goteborg (2011)
24. Falcone, P., Borrelli, F., Asgari, J., Tseng, H.E., Hrovat, D.: Linear time varying model predictive control and its application to active steering systems: stability analysis and experimental validation. Int. J. Rob. Nonlinear Control. **18**, 862–875 (2008)
25. Bhat, S.P., Dennis, S.B.: Geometric homogeneity with applications to finite-time stability: Math. Control, Signals and Syst. **17**, 101–127 (2005)
26. Roshanbin, A., Naraghi, M.: Vehicle integrated control-an adaptive optimal approach to distribution of tire forces. In: Presented at 2008 IEEE International Conference on Networking, Sensing and Control, Sanya, 6–8 (April 2008)

27. Li, Y.: Robust Control: Linear Matrix Inequality Processing Method. Tsinghua University Press, Beijing (2002)
28. Tian, B.: Multivariable finite time attitude control for quadrotor UAV: theory and experimentation. IEEE Trans. Ind. Electron. **65**, 2567–2577 (2018)
29. Elobaid, Y.M.T., Huang, J., Wang, Y.: Nonlinear disturbance observer based robust tracking control of pneumatic muscle. Math. Probl. Eng. **2014**, 1–8 (2014)

Yuwei Tong received the B.E. degree in automobile service engineering from Chuzhou University, Chuzhou, China, in 2019. He is currently pursuing the M.S. degree in Mechanical Engineering from the Guilin University of Electronic Technology, Guilin, China. His research interests include vehicle dynamics control and vehicle platoon control

Cong Li received the M.S. degree in Mechanical Engineering from the Guilin University of Electronic Technology in 2010. She is currently associate professor with the School of Mechanical Engineering, Guilin University of Aerospace Technology. Her research interests include electric vehicle, expert systems and robust control

Gang Wang received the Ph.D. degree in mechanical engineering from the School of Mechanical Engineering, Shenyang University of Technology, Shenyang, China, in 2017. He is currently a Lecturer with School of Mechanical and Electrical Engineering, Guilin University of Electronic Technology, Guilin, China. His current research interests include control of active suspension systems and active mass damper

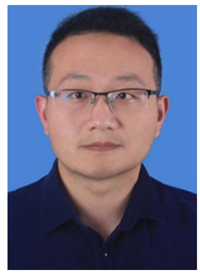

Hui Jing Full Professor in Guilin University of Electronic Technology. He received the PhD degree in automotive engineering from Southeast University in 2017. Later, he did postdoctoral research in Shanghai Jiao Tong University. His research interests are related to vehicle dynamics and control, autonomous driving and robust control